
Performance Characteristics of the Biograph Vision Quadra PET/CT System with a Long Axial Field of View Using the NEMA NU 2-2018 Standard

George A. Prenosil¹, Hasan Sari^{1,2}, Markus Fürstner¹, Ali Afshar-Oromieh¹, Kuangyu Shi¹, Axel Rominger¹, and Michael Hentschel¹

¹Department of Nuclear Medicine, Bern University Hospital, University of Bern, Bern, Switzerland; and ²Advanced Clinical Imaging Technology, Siemens Healthcare AG, Lausanne, Switzerland

Our purpose was to evaluate the performance of the Biograph Vision Quadra PET/CT system. This new system is based on the Biograph Vision 600, using the same silicon photomultiplier-based detectors with $3.2 \times 3.2 \times 20$ mm lutetium-oxoorthosilicate crystals. The 32 detector rings of the Quadra provide a 4-fold larger axial field of view (AFOV) of 106 cm, enabling imaging of major organs in 1 bed position.

Methods: The physical performance of the scanner was evaluated according to the National Electrical Manufacturers Association NU 2-2018 standard, with additional experiments to characterize energy resolution. Image quality was assessed with foreground-to-background ratios of 4:1 and 8:1. Additionally, a clinical ¹⁸F-FDG PET study was reconstructed with varying frame durations. In all experiments, data were acquired using the maximum ring distance of 322 crystals (MRD 322), whereas image reconstructions could be performed with a maximum ring distance of only 85 crystals (MRD 85). **Results:** The spatial resolution at full width at half maximum in the radial, tangential, and axial directions was 3.3, 3.4, and 3.8 mm, respectively. The sensitivity was 83 cps/kBq for MRD 85 and 176 cps/kBq for MRD 322. The noise-equivalent count rates (NECRs) at peak were 1,613 kcps for MRD 85 and 2,956 kcps for MRD 322, both at 27.49 kBq/mL. The respective scatter fractions at peak NECR equaled 36% and 37%. The time-of-flight resolution at peak NECR was 228 ps for MRD 85 and 230 ps for MRD 322. Image contrast recovery ranged from 69.6% to 86.9% for 4:1 contrast ratios and from 77.7% to 92.6% for 8:1 contrast ratios reconstructed using point-spread function time of flight with 8 iterations and 5 subsets. Thirty-second frames provided readable lesion detectability and acceptable noise levels in clinical images.

Conclusion: The Biograph Vision Quadra PET/CT device has spatial and time resolution similar to those of the Biograph Vision 600 but exhibits improved sensitivity and NECR because of its extended AFOV. The reported spatial resolution, time resolution, and sensitivity make it a competitive new device in the class of PET scanners with an extended AFOV.

Key Words: acceptance test; long field of view; total-body; NEMA; digital PET

J Nucl Med 2022; 63:476–484
DOI: 10.2967/jnumed.121.261972

Over the last few decades, PET in combination with CT has consolidated and expanded its role as a standard-of-care imaging modality in many clinical fields. This growth in use went hand in hand with technologic progress, such as the exploitation of faster scintillators and improved time-of-flight (TOF) performance (1), an extended field of view (FOV), and resolution recovery methods for image reconstruction (2).

Recently, digital PET (3,4) replaced bulky photomultiplier tubes with silicon photomultipliers (SiPM), using single-photon avalanche diodes operating in Geiger mode to detect scintillation photons generated from transferring the energy of annihilation photons in the scintillator. SiPMs not only are smaller than photomultiplier tubes but also provide a 1,000 times larger gain and increased energy resolution (5). Thanks to high amplification, a fast signal, and high light collection, SiPM-based PET systems achieve a time resolution of as low as 214 ps (6), compared with the 540 ps of PET systems using photomultiplier tubes (7,8). When SiPMs are directly coupled to a fast scintillator such as lutetium-oxoorthosilicate, the resulting excellent TOF increases PET sensitivity and reduces noise; in conjunction with small-size crystals, the TOF gain provides improved image resolution, improved detectability, and reduced image noise (6,9). The sensitivity gain can be used to reduce the administered radioactivity dose or to shorten the acquisition duration (10,11).

Current clinical PET/CT systems typically cover an axial FOV (AFOV) of about 15–26 cm. As a result, only about 1%–3% of the possible positron/electron annihilation events produce coincidence lines of response (LORs) that are actually detected. Furthermore, in many clinical scenarios, time-consuming multiple bed positions must be imaged to cover the relevant portion of the patient. Stretching the FOV by axially spacing out the detector rings increases coverage of the patient body but not the overall sensitivity (12). The viable solution is to increase the number of detector rings, with the accompanying down side of increased costs (13). The Explorer consortium and United Imaging Healthcare Shanghai, in collaboration with the University of California Davis team (14–16), the University of Pennsylvania (17), and Siemens Healthineers (18,19), all developed systems with long AFOVs, covering an axial length spanning from 64 to 194 cm. The Biograph Vision Quadra from Siemens Healthineers is a commercially available PET/CT system that combines SiPM detector technology with an optimal (13,15,18) nearly total-body coverage (106-cm AFOV). Essentially, the Biograph Vision Quadra comprises the equivalent of 4 axially concatenated PET subsystems of

Received Jan. 26, 2021; revision accepted May 25, 2021.
For correspondence or reprints, contact George A. Prenosil (george.prenosil@insel.ch).
Published online Jul. 22, 2021.
COPYRIGHT © 2022 by the Society of Nuclear Medicine and Molecular Imaging.

Biograph Vision 600 PET/CT systems, building on proven high-spatial-resolution and high-time-resolution technology (6,20).

The development of long-AFOV PET/CT scanners offers a great opportunity to improve clinical workflow and explore new applications (13,15,18). The high sensitivity allows for a very low dose or very fast scans (21) (with higher throughput, better patient comfort, and fewer motion artifacts) in today's clinical routine. In terms of new applications, a high sensitivity and simultaneous coverage of multiple organs enables, among other new research topics, low-count imaging (monoclonal antibody imaging or cell tracking), multiorgan interaction studies (e.g., brain–gut or brain–spine), parametric imaging, and pharmaceutical kinetics investigations.

Even though human imaging studies had been performed earlier on a total-body PET device (16,21), comparable standardized performance data for the uEXPLORER (United Imaging Healthcare) with an AFOV of 194 cm (22) and the PennPET Explorer with an AFOV of 64 cm (17) were published only very recently.

Published first in 1994 (23) by the National Electrical Manufacturers Association (NEMA), the NEMA NU 2 standards quickly became the accepted set of measurements for benchmarking commercial PET/CT systems. The aim of this study was therefore to evaluate the performance of the new commercially available long-AFOV Biograph Vision Quadra PET/CT system according to the latest NEMA NU 2-2018 standard (24). The measurements included spatial resolution, scatter fraction, noise-equivalent count rate (NECR), sensitivity, correction accuracy, PET and CT coregistration accuracy, image quality, and TOF resolution. Furthermore, the energy resolution of the scanner is reported, and clinical images from one of the initial patient studies are illustrated.

MATERIALS AND METHODS

Biograph Vision Quadra PET/CT System Specifications

The Biograph Vision Quadra uses the technology previously developed for the Biograph Vision 600 PET/CT system (6,20). The lutetium-oxoorthosilicate crystals are directly coupled to an SiPM array with 16 output channels. Eight mini blocks form a detector block, with 2 adjacent detector blocks always sharing a common electronic unit. The Biograph Vision Quadra has 4 times the number of detector rings found in the Biograph Vision, with a total axial span of 320 crystals. This arrangement gives the Biograph Vision Quadra an AFOV of 106 cm, versus 26.3 cm in the Biograph Vision 600 (7). Table 1 details more system specifications.

The Biograph Vision Quadra records all possible LORs using its maximum full-ring difference (MRD) of 322 crystal rings (MRD 322), with an acceptance angle of 52°. In this first version of the reconstruction software (VR10), also named high-sensitivity mode, images are reconstructed with LORs spanning an MRD of 85 crystal rings (MRD 85). This MRD is comparable to the Biograph Vision MRD of 79 (7), corresponding to an acceptance angle for axial LOR of about 18°. The MRD metric refers to the number of crystals in the LOR's axial extent and includes the gaps between blocks. In MRD 85 mode, the Vision Quadra does not use all the possible LORs between scintillating crystals for image reconstruction. In this work, all data were acquired using MRD 322, whereas image reconstructions were performed using only MRD 85. For experiments requiring no image reconstruction, results for MRD 85 and MRD 322 are reported side by side. Although currently unsuitable for clinical application, MRD 322 measurements are still useful in a scientific context.

Performance Measurements

The performance of the Biograph Vision Quadra PET/CT system installed at the nuclear medicine department of the Inselspital Bern

TABLE 1
Biograph Vision Quadra System Specifications

Parameter	Specification
Crystal size	3.2 × 3.2 × 20 mm
Crystals per SiPM (mini block)	5 × 5
Detector blocks per ring	38
Detector ring diameter	82 cm
Energy window	435 keV–585 keV
PET AFOV	106 cm
CT model	Siemens Definition Edge
CT slices	128
Bore length with CT	230 cm
Maximal patient weight	227 kg
Cooling water temperature	4°C–12°C
SiPM array size	16 × 16 mm
Mini blocks per detector block	2 × 4
Detector rings	32
Image plane spacing	1.65 mm
Coincidence time window	4.7 ns
PET transaxial FOV	78 cm
CT generator power	100 kW
CT minimal slice spacing	0.5 mm
Total system length	611 cm
System weight	5934 kg
Operating room temperature	18°C–28°C

was benchmarked according to the NEMA NU 2-2018 standard (24). Additionally, we measured the system's energy resolution, which is not part of the NEMA 2018 measurement set. Data were analyzed using the NEMA tools software (Siemens Healthineers).

In addition, PET images from a human study are presented to illustrate image quality together with some initial quantification results. All PET images in this work were reconstructed into a matrix of 440 × 440 × 645 with an isotropic voxel spacing of 1.65 mm. This is also the innate sampling resolution of the Quadra PET/CT.

Spatial Resolution. Spatial resolution was measured at 6 different positions (Table 2; Supplemental Fig. 1; supplemental materials are available at <http://jnm.snmjournals.org>) using a point source with a 0.25-mm diameter containing 393 kBq of ²²Na (Eckert and Ziegler).

After acquiring at least 4 × 10⁶ true counts for every position, images were reconstructed in MRD 85, without the use of a postreconstruction filter, and with 3-dimensional TOF direct inversion Fourier transform backprojection, an analytic backprojection reconstruction method (18). Corrections were applied for detector normalization, dead time, radial-arc-correction decay, and randoms, but no scatter or attenuation correction was used.

Resolution was reported as the full width at half maximum and full width at tenth maximum of the point source's spread in the radial, tangential, and axial directions. For each direction, average values over the 2 axial positions were calculated.

Count Rates: Trues, Randoms, Scatters, and NECRs. For count rate measurements, we used a solid polyethylene cylinder with an outside diameter of 20.3 cm and a 700-cm length. A 3-mm-wide and 70-cm-long polyethylene capillary was filled with 894 MBq of ¹⁸F and inserted into a 6.4-mm-wide hole running parallel to the central axis of the cylinder at a radial offset of 45 mm.

TABLE 2
Spatial Resolution in MRD 85 Mode

Axial position (cm)	Radial position (cm)	Full width at half-maximum (mm)			Full width at tenth maximum (mm)		
		Radial	Tangential	Axial	Radial	Tangential	Axial
13.3 (1/8 of FOV)	1	3.19	3.58	3.78	6.49	7.15	7.63
13.3 (1/8 of FOV)	10	4.38	3.47	3.84	8.22	6.88	7.74
13.3 (1/8 of FOV)	20	5.82	3.12	4.21	10.71	6.25	8.87
53.0 (1/2 of FOV)	1	3.35	3.31	3.77	6.47	6.33	7.62
53.0 (1/2 of FOV)	10	4.38	3.53	3.90	8.19	6.81	7.80
53.0 (1/2 of FOV)	20	5.84	3.33	4.27	10.82	6.24	9.06
Average 1/2 and 1/8	1	3.27	3.44	3.77	6.48	6.74	7.63
Average 1/2 and 1/8	10	4.38	3.50	3.87	8.20	6.85	7.77
Average 1/2 and 1/8	20	5.83	3.22	4.24	10.77	6.25	8.96

The cylinder phantom was placed onto the patient table in the center of the FOV and axially aligned with the PET/CT system. The line source insert was positioned close to the patient table, and foam blocks were used to elevate the phantom above the table to an axially aligned position. Data acquisitions in list mode were performed over the course of 700 min. However, the NEMA NU 2 criterion of waiting until true-event losses are less than 1.0% could not be achieved because of the intrinsic radioactivity of lutetium-oxoorthosilicate. Therefore, a previously described different methodology had to be used (25): count rates were measured using delayed coincidence windows, and the scatter fraction was calculated as a function of count rate.

Every 20 min, data were acquired for 240 s, and the acquisitions were binned into 35 individual sinograms of equal duration. Data were not corrected for variations in detector sensitivity, randoms, scatter, dead time, or attenuation effects.

Rates of total, true, scatter, and noise-equivalent counts were calculated as specified by section 4 of the NEMA NU 2-2018 protocol. Prompt and random sinograms were generated for each acquisition and each slice. Because of the extended AFOV of the Quadra, only slices within the central 65 cm of the AFOV were used for histogram generation.

Sensitivity. For sensitivity measurements, we used the same 70-cm-long polyethylene capillary as described above and filled it over a total length of 68 cm with an aqueous solution of 4.56 MBq of ^{18}F . The line source was surrounded by 5 concentric aluminum sleeves of matching length and with known radiation attenuation. The setup was bedded on foam holders with negligible attenuation. One sensitivity measurement series was performed with the capillary axially aligned at the center of the AFOV, and the other series was performed with a 10-cm radial offset added to the first placement. The supports for the capillary stayed outside the FOV. By measuring the count rate while consecutively removing sleeves, we extrapolated the attenuation-free count rate, for example, the count rate of the naked line source (26). Data were acquired for 300 s for each sleeve.

Accuracy: Correction for Count Losses and Randoms. Data acquired for count rate measurements were used to estimate the accuracy of the correction of count losses due to detector dead time and due to random counts (randoms). Corrections for randoms, scatter, dead time, and attenuation were applied. For attenuation correction, a low-dose CT scan of the phantom was acquired with a 120-keV tube voltage, a 80-mAs tube current, and a pitch of 0.8. The CT image was

reconstructed into a 512×512 matrix. Scatter was corrected for as described by Watson (27).

The PET image was reconstructed from MRD 85 data using ordered-subsets expectation maximization (OSEM)-TOF with 4 iterations, 5 subsets, and 2-mm gaussian postreconstruction filtering.

Image Quality, Accuracy of Corrections. A NEMA International Electrotechnical Commission body phantom (28) of 180-mm interior length was used for assessing image quality and the accuracy of attenuation and scatter corrections. The gravimetrically determined volume of the background compartment was 9,742 mL, and the fillable 6 spheres had internal diameters of 10, 13, 17, 22, 28, and 37 mm. The central lung insert filled with polystyrene beads was void of any activity.

The background activity concentration of ^{18}F was 5.3 kBq/mL at the start of image acquisition, constituting our low-activity-concentration benchmark. A first measurement was taken with all spheres filled with a concentration 4 times that of the background as stated in the NEMA NU 2-2018 protocol (24). A second measurement was taken with a concentration 8 times that of the background. The phantom was axially aligned, with the spheres positioned around the center of the FOV. The cylindrical scatter phantom was positioned adjacent to the sphere-containing phantom, and its line source was filled with 100 MBq of ^{18}F at the start of the acquisition.

A single bed position was acquired for 30 min in list mode. Data were corrected for decay, normalization, scatter, randoms, and attenuation. The required attenuation CT scan was acquired before the PET measurements as described above. Images were reconstructed in MRD 85 using OSEM-TOF and point-spread function (PSF)-TOF with 8 iterations and 5 subsets. Both reconstructions were also performed using 4 iterations and 5 subsets. No postreconstruction filtering was applied. Activity spill-in into the cold lung insert was used to calculate an average residual error.

TOF and Energy Resolution. To measure the positional uncertainty of the coincidence event localization, we used the same CT and PET data as previously acquired for the NECR experiment, without corrections applied.

To determine the position of the line source, the first frame with activity below the peak NECR was reconstructed in MRD 85 using OSEM with 10 iterations and 5 subsets, with scatter, random, and attenuation correction but without decay correction. The method to calculate TOF resolution is described in section 8 of the NEMA NU-2 2018 standard and was also described by Wang et al. (29).

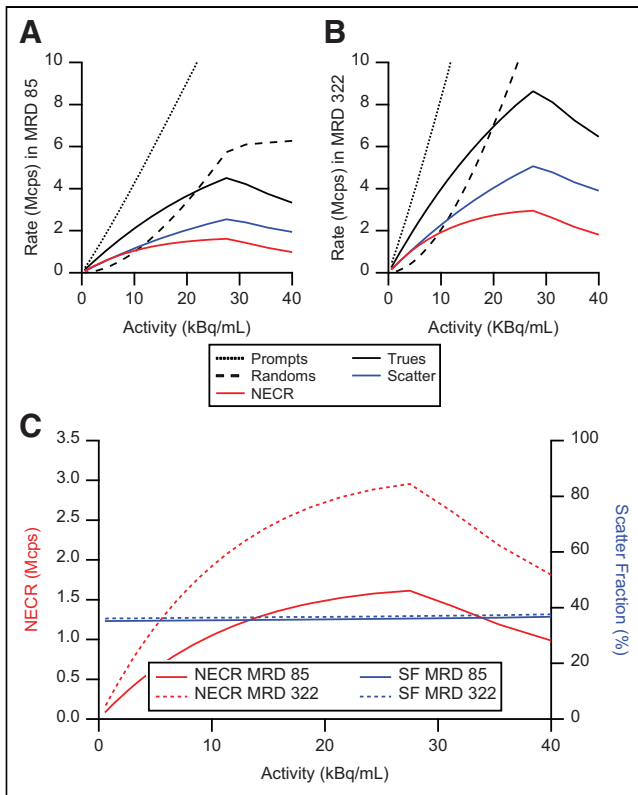


FIGURE 1. (A and B) Plots of prompts, randoms, trues, scatter, and NECRs for MRD 85 (A) and MRD 322 (B). (C) NECR and scatter fractions (SF).

For measuring the energy resolution of the scanner, we used the same data but without any corrections applied. This measurement is not part of the NEMA NU 2-2018 standard, but it is based on the same method as for the TOF resolution and was previously described (30). An image reconstruction was performed for determining the line source centroid, with scatter, random, and attenuation correction but without decay correction. Trues were assumed to be within a perpendicular distance of ± 20 mm of line source data, and thus counts at ± 20 mm were assumed to come from scatter, randoms, and background. For each crystal, an energy histogram was generated using all events within a distance of -20 and $+20$ mm. The weighted combination of counts at -20 mm and $+20$ mm, as done in NEMA count-rate

TABLE 3

Count Rates, TOF Resolution, Energy Resolution $\times 100\%$ = 511 keV

Parameter	MRD 85	MRD 322
Peak NECR (kcps @ kBq/mL)	1,613 @ 27.49	2,956 @ 27.49
Peak true rate (kcps @ kBq/mL)	4,501 @ 27.49	8,633 @ 27.49
Scatter fraction @ peak NECR (%)	36	37
TOF resolution @ peak NECR (ps)	228	230
TOF resolution @ 5.3 kBq/mL (ps)	225	228

TABLE 4
Sensitivity

Radial offset (cm)	Sensitivity (cps/kBq)	
	MRD 85	MRD 322
0	82.6	175.3
10	84.1	176.7
0 and 10 average	83.4	176.0

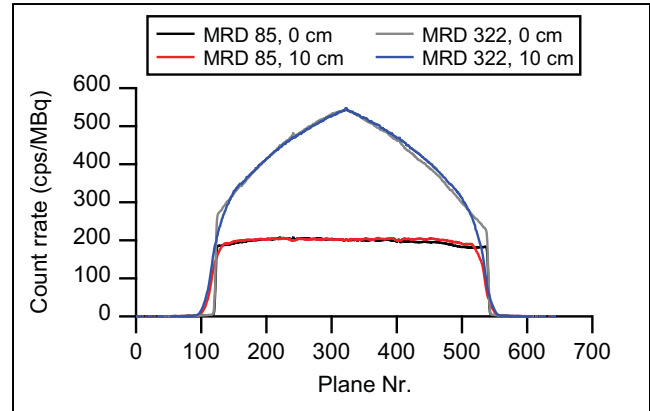


FIGURE 2. Axial sensitivity profiles for 0- and 10-cm radial offset positions and for both MRD modes.

studies, was used to estimate the background (scatter and randoms). All crystal peaks were aligned and added in a common energy histogram (Supplemental Fig. 2). The energy resolution was defined as the full width at half maximum of the energy spectrum so obtained. For comparison, the energy resolution was also measured using a more conventional method, by placing a 19-cm-long line source containing 19.19 MBq of ^{68}Ge without a scattering medium at the center of the FOV.

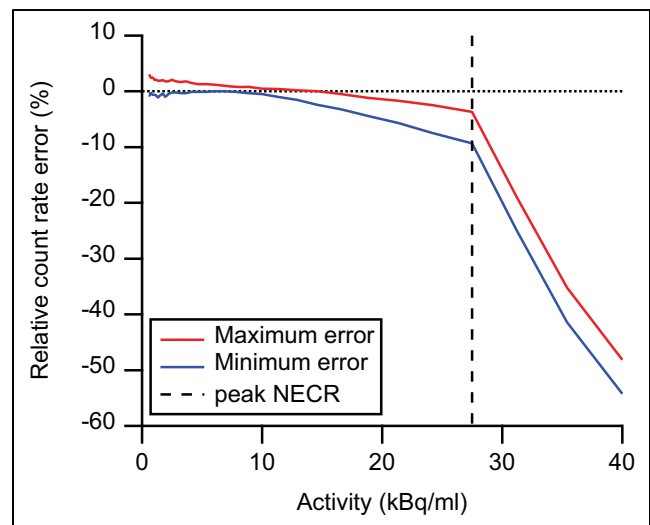


FIGURE 3. Maximum and minimum relative count rate error in MRD 85 vs. activity concentration; dashed line highlights values at peak NECR.

TABLE 5

Image Quality Measurements Reconstructed with OSEM-TOF Using 8 Iterations and 5 Subsets or Using 4 Iterations and 5 Subsets

Sphere diameter	4: 1 sphere-to-background ratio		8: 1 sphere-to-background ratio	
	Contrast recovery (%)	Background variability (%)	Contrast recovery (%)	Background variability (%)
8 iterations, 5 subsets				
10	60.11	3.19	64.07	2.73
13	64.52	2.58	70.88	2.37
17	74.33	1.87	82.60	1.85
22	78.02	1.52	84.45	1.41
28	82.83	1.27	87.88	1.01
37	85.23	0.99	91.05	0.87
Average lung residual error (%)	2.41		2.55	
4 iterations, 5 subsets				
10	56.35	2.46	61.95	2.14
13	61.52	2.04	68.99	1.88
17	72.26	1.54	80.94	1.51
22	76.33	1.28	83.09	1.2
28	81.35	1.1	86.69	0.91
37	84.24	0.9	90.16	0.81
Average lung residual error (%)	4.89		5.13	

TABLE 6

Image Quality Measurements Reconstructed with PSF-TOF Using 8 Iterations and 5 Subsets or Using 4 Iterations and 5 Subsets

Sphere diameter	4: 1 sphere-to-background ratio		8: 1 sphere-to-background ratio	
	Contrast recovery (%)	Background variability (%)	Contrast recovery (%)	Background variability (%)
8 iterations, 5 subsets				
10	74.44	2.38	77.65	2.24
13	69.56	1.93	74.81	1.90
17	76.98	1.52	86.37	1.52
22	80.56	1.23	87.88	1.21
28	84.44	0.99	90.18	0.91
37	86.86	0.82	92.59	0.84
Average lung residual error (%)	2.34		2.48	
4 iterations, 5 subsets				
10	64.25	1.67	74.40	1.49
13	67.88	1.4	74.73	1.34
17	74.6	1.15	82.73	1.15
22	77.66	0.97	85.37	0.96
28	82.38	0.83	88.54	0.80
37	85.47	0.76	91.19	0.80
Average lung residual error (%)	4.84		5.09	

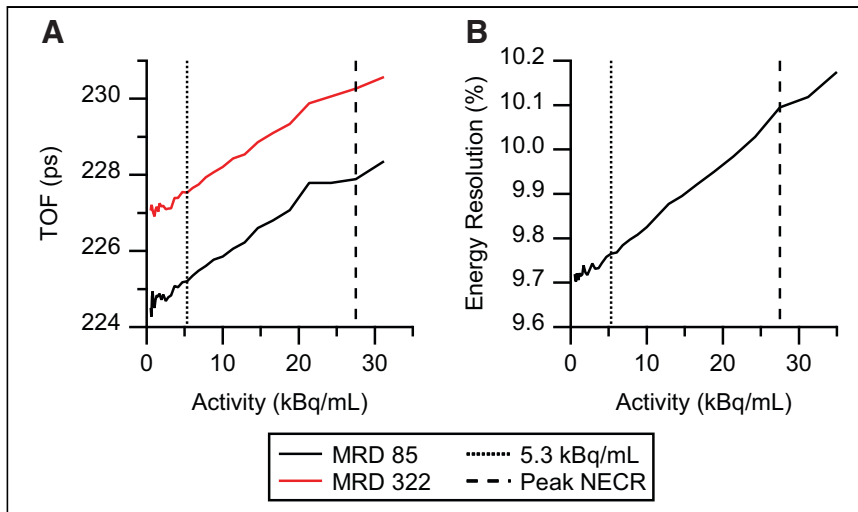


FIGURE 4. TOF (A) and energy resolution (B) as function of activity concentration, with low and peak NECR activity concentration marked with dashed lines.

PET/CT Coregistration Accuracy. Coregistration accuracy between the PET and the CT images was measured with a vial of 13.3-mm diameter and conical bottom and filled with an aqueous solution of 0.2 mL of 370-MBq ^{18}F and 1 mL of CT contrast medium (Ultravist 370; Bayer Vital) according to the NEMA NU 2-2018 document (24). CT images were reconstructed into a 512×512 matrix and slice thickness of 0.6 mm, and PET images were reconstructed using OSEM-TOF with 10 iterations and 5 subsets, without attenuation correction or postreconstruction filtering.

Human Studies. An oncologic female patient (age, 81 y; height, 160 cm; weight, 57 kg) participating in a clinical study (31) was scanned 60 min after administration of 191 MBq of ^{18}F -FDG. A single bed position was acquired for 10 min. Eight images were reconstructed by binning the list-mode data into 10-min, 6-min, 4-min, 3-min, 2-min, 1-min, 30-s, and 15-s frames. Images were reconstructed using PSF-TOF with 4 iterations, 5 subsets, and a gaussian postprocessing filter of 2 mm in full width at half maximum.

An isocontour threshold of 40% delineated the volume of interest of an ^{18}F -FDG-avid lesion in the 10-min frame, and a spheric volume of interest with a diameter of 5.1 cm was placed in the center of the liver in the same frame. Both volumes of interest were then copied into the remaining frames. SUVs and coefficients of variation were computed for each volume of interest in every frame.

The human study (31) had been approved by the regional ethics committee, and the patient had signed an informed consent form.

RESULTS

Spatial Resolution

Table 2 reports the full width at half maximum and full width at tenth maximum for the 6 different positions in MRD 85 mode.

Count Rates: Trues, Randoms, Scatters, and Noise-Equivalent Counts

Figure 1 shows count rate plots for trues, randoms, scatter, and noise-equivalent counts measured at MRD 85 and MRD 322, as well as for scatter fractions at peak NECR. Table 3 summarizes the count rate findings. As all events were recorded regardless of the MRD setting, the peak NECR of 1,613 kcps for MRD 85 and of 2,956 kcps for MRD 322 were both observed at 27.49 kBq/mL.

Sensitivity

Table 4 reports total sensitivities measured for the Biograph Vision Quadra for both MRD modes. The average system sensitivities are 83.4 cps/kBq for MRD 85 and 176.0 cps/kBq for MRD 322.

Figure 2 exhibits the axial sensitivity profiles. Although MRD 85 provides for homogeneous sensitivity of around 200 cps/MBq over the measured AFOV, MRD 322 shows a peak of 549 cps/MBq in the middle of the AFOV. As expected, the MRD 85 mode gives the Biograph Vision Quadra a flat sensitivity similar to the peak sensitivity of the Biograph Vision 600 (6). In MRD 322 mode, the axial peak sensitivity of the Biograph Vision Quadra is 2.75 times higher than the axial peak sensitivity of the Biograph Vision 600 (6).

Accuracy: Correction for Count Losses and Randoms

Accuracy measurements were obtained from the difference between expected and measured activity concentration on the PET data as previously acquired for the NECR in MRD 85. Figure 3 shows the minimum and maximum error in the PET image plotted against activity concentration. The count rate errors were below 5% (maximum) and 10% (minimum), up to the peak NECR; after this discontinuity, both error curves increased their negative slopes by a factor of 20.

Image Quality, Accuracy of Corrections

Table 5 reports the contrast recovery, relative background variability, and lung residual error for images reconstructed with OSEM-TOF for the 2 sphere-to-background ratios examined, and Table 6 reports the same for images reconstructed with PSF-TOF.

TOF and Energy Resolution

The TOF resolution at peak NECR was 228 ps for MRD 85 and 230 ps for MRD 322. At a low (background) activity concentration of 5.3 kBq/mL, the TOF resolutions were 225 and 228 ps, respectively (Table 3). Figure 4 shows the time resolution over the whole activity range.

Calculated energy resolution in MRD 85 mode was 10.1% at peak NECR and 9.8% at 5.30 kBq/mL (Fig. 4B). When measured using the ^{68}Ge line source, energy resolution was 8.9% at peak NECR, slightly better because of the absence of scattered photons. This value was almost identical to the 9.0% published for the Biograph Vision 600 (20).

PET/CT Coregistration Accuracy

The maximum coregistration error was +1.38 mm. Supplemental Table 1 reports the 6 individual coregistration measurements.

Human Studies

Excellent quality was observed in ^{18}F -FDG images reconstructed with longer frame durations, with slightly higher noise seen in frames reconstructed with 30 s and 15 s (Fig. 5). The evaluated lesion had a diameter of 1.58 cm and was detectable in all 8 frames. However, image noise started to become a problem in

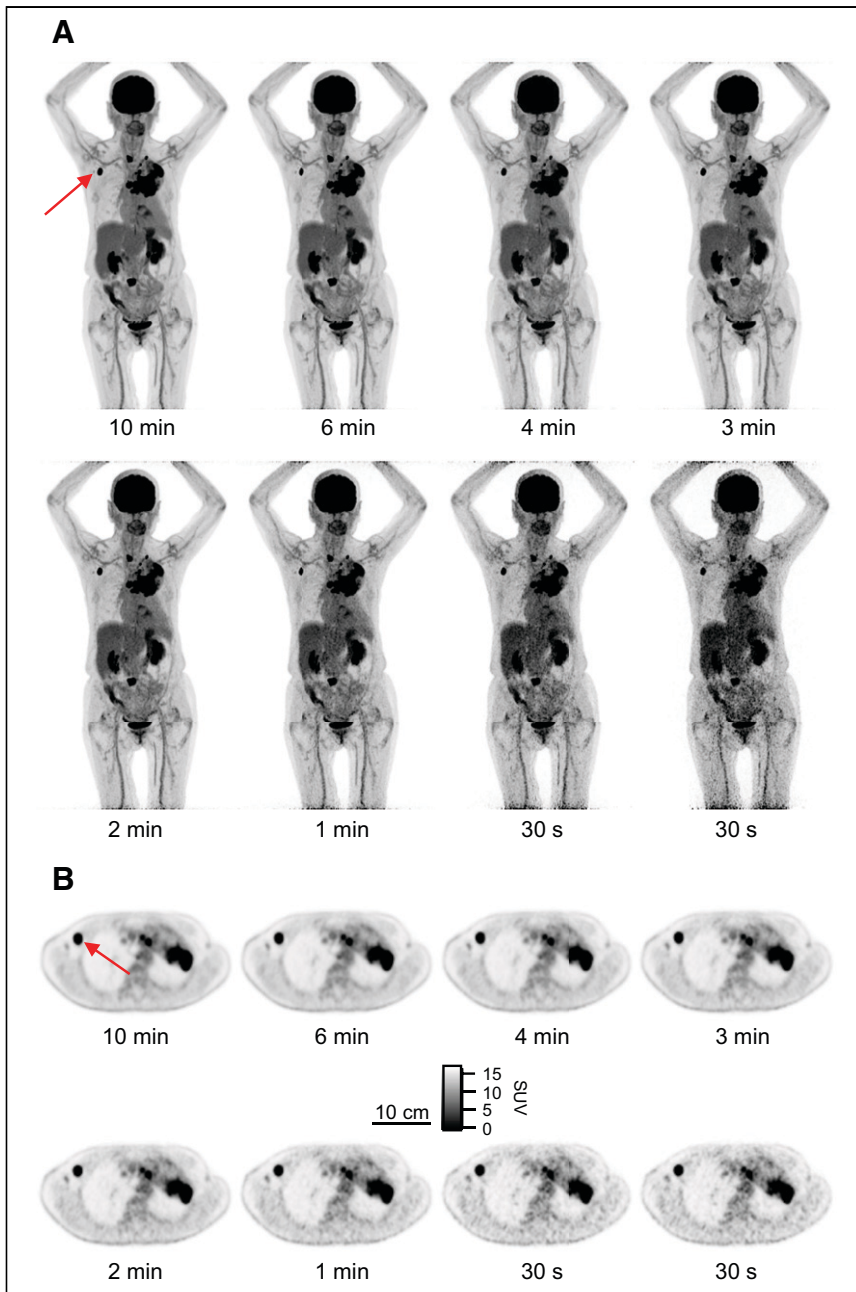


FIGURE 5. (A) Maximum-intensity PET projections of oncologic patient, reconstructed with different frame durations. (B) Axial PET images. Arrows indicate reported lesion.

the 15-s frame, with a lesion coefficient of variation of 0.52 and a liver coefficient of variation of 0.22.

Figure 6A shows the SUVs within the tumor and liver for each frame duration. The coefficient-of-variation log-log plots show the expected power law with respect to frame duration (Fig. 6B).

DISCUSSION

No significant difference in spatial resolution was found between our data from the Biograph Vision Quadra and previously published data from the Biograph Vision (paired Wilcoxon

signed-ranked test) (6). This similarity is to be expected since crystal and detector size, geometry, and readout are the same in both scanners.

The NEMA NECRs at peak were 1,613 kcps for MRD 85 and 2,956 kcps for MRD 322, with both peaks occurring at 27.49 kBq/mL. The NECR curve (Fig. 1) has a discontinuity and drops after the peak, when the count rate reaches the maximum total-event throughput supported by the hardware (19), which is around 129 Mcps. This occurs even far above actual clinical (31) or even high-count regimes (20).

The NEMA sensitivities were 83.4 cps/kBq and 176 cps/kBq for MRD 85 and MRD 322, respectively. As a comparison, the Biograph Vision 600 has a sensitivity at the center of 16.4 cps/kBq and a peak NECR of 306 kcps: the Biograph Quadra provides a NEMA sensitivity that is about 5 times that of the Biograph Vision in MRD 85 and about 10 times in MRD 322 mode (6). In fact, the NEMA sensitivity of the Biograph Quadra for MRD 322 is on a par with the uEXPLORER (22), a finding that is not surprising, given the size of the source and the 2 scanners' similar acceptance angles for axial LORs.

The TOF resolution was 225 ps for MRD 85 and 227 ps for MRD 322. The measured time resolution on the Quadra was slightly worse than the published value for Vision 600 (6), possibly because of nonuniformity of detector and signal sync over a larger number of detectors and electronic modules and a time alignment method that is not yet optimized. In fact, both time and energy resolution of the scanner are stable with count rate, exhibiting a change of only 2%–3% over the whole count rate range.

This high time resolution functions as an additional equivalent-counts amplifier, which allows the effective sensitivity to increase by a TOF gain factor of about $D/(\Delta t \times c/2)$, according to the standard TOF gain model (where D is size of the patient, Δt is the time resolution, and c is the speed of light). Better TOF resolution translates into lower image noise at an equal number of counts and a higher robustness of the reconstruction (10,32,33) than for PET scanners with similar NEMA sensitivity but poorer time resolution.

Because we followed the NEMA NU 2-2018 protocol and not the NEMA NU 2-2012, only the results for the 4 smallest spheres are comparable to those published for the Biograph Vision 600 (6). The contrast was comparable to those of the 4 spheres reconstructed with PSF-TOF, but background variability was around 2.5 times lower for the Quadra (6). This finding can be explained by the fact that the Quadra has a sensitivity 5 times higher at equal

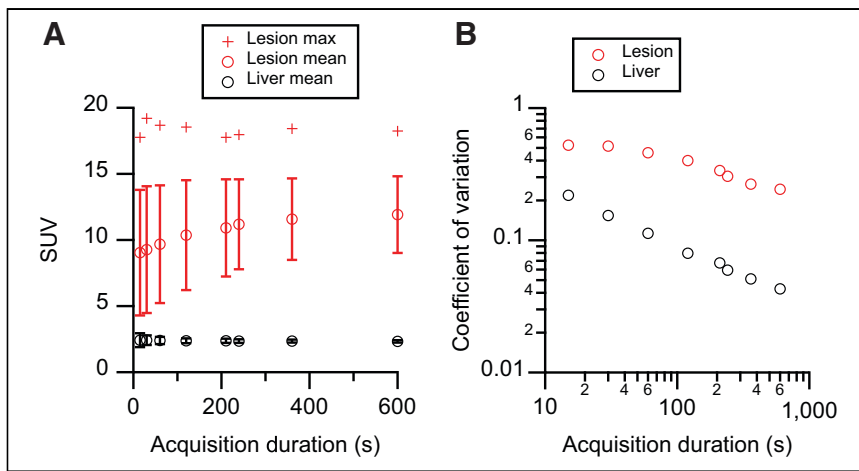


FIGURE 6. Tumor and liver SUVs (A) and coefficients of variation (B) of oncologic patient. Mean values \pm SD are reported.

KEY POINTS

QUESTION: What are the performance characteristics of the Biograph Vision Quadra total-body PET/CT system according to the NEMA NU 2-2018 standard?

PERTINENT FINDINGS: The Biograph Vision Quadra has a spatial resolution similar to that of the Biograph Vision 600, but because of the extended AFOV, has an NECR 5 to 10 times higher a peak sensitivity up to 2.75 times higher.

IMPLICATIONS FOR PATIENT CARE: The increased sensitivity of the Biograph Vision Quadra allows for total-body imaging with a reduced injected dose or a reduced acquisition duration, and dynamic studies can be conducted with high spatial and high temporal resolution.

spatial resolution. As previously shown for the Biograph Vision 600 (6), Gibbs artifacts increase contrast in the smallest sphere, a well-known characteristic of resolution recovery or PSF reconstruction (34). All images were reconstructed with the MRD 85 mode's low sensitivity, leading to a contrast-to-noise ratio that is lower than possible. In a future software update, the ultra-high-sensitivity mode will be available with MRD 322, in which all LORs spanning the full AFOV will be used in image reconstruction. However, the impact of oblique LORs on image quality remains to be examined.

From the patient images, we expect that clinical acquisitions below 2 min will be able to provide acceptable image quality when the Quadra is used. Besides exploiting the increased sensitivity of the system for reductions in injected dose, delayed or prolonged imaging regimes are also conceivable (31). Additionally, the Quadra is suited for temporally and spatially well-resolved dynamic studies that cover the entire upper body.

CONCLUSION

The Biograph Vision Quadra PET/CT has spatial and time resolution similar to those of the PET/CT Biograph Vision 600 but exhibits improved sensitivity and NECR ($\times 5$ or $\times 10$, depending on MRD mode) because of the extended AFOV. The high time resolution allows for state-of-the-art noise-reducing TOF reconstructions. The combination of high spatial resolution, high time resolution, and very high sensitivity makes the Quadra a high-performance new device in the class of total-body PET scanners.

DISCLOSURE

Hasan Sari is a full-time employee of Siemens Healthcare AG, Switzerland. No other potential conflict of interest relevant to this article was reported.

ACKNOWLEDGMENTS

Thanks go to Kevin Lohmann and Colin Ward for assistance with the PET measurements. We also thank Maurizio Conti and Bernard Bendriem for their useful discussions.

REFERENCES

1. Surti S, Kuhn A, Werner ME, Perkins AE, Kolthammer J, Karp JS. Performance of Philips Gemini TF PET/CT scanner with special consideration for its time-of-flight imaging capabilities. *J Nucl Med.* 2007;48:471–480.
2. Jakoby BW, Bercier Y, Watson CC, Bendriem B, Townsend DW. Performance characteristics of a new LSO PET/CT scanner with extended axial field-of-view and PSF reconstruction. *IEEE Trans Nucl Sci.* 2009;56:633–639.
3. Koopman D, Groot Koerkamp M, Jager PL, et al. Digital PET compliance to EARL accreditation specifications. *EJNMMI Phys.* 2017;4:9.
4. Nguyen NC, Vercher-Conejero JL, Sattar A, et al. Image quality and diagnostic performance of a digital PET prototype in patients with oncologic diseases: initial experience and comparison with analog PET. *J Nucl Med.* 2015;56:1378–1385.
5. Bisogni MG, Del Guerra A, Belcarì N. Medical applications of silicon photomultipliers. *Nucl Instrum Methods Phys Res A.* 2019;926:118–128.
6. van Sluis J, de Jong J, Schaar J, et al. Performance characteristics of the digital Biograph Vision PET/CT system. *J Nucl Med.* 2019;60:1031–1036.
7. Carlier T, Ferrer L, Conti M, et al. From a PMT-based to a SiPM-based PET system: a study to define matched acquisition/reconstruction parameters and NEMA performance of the Biograph Vision 450. *EJNMMI Phys.* 2020;7:55.
8. Gnesin S, Kieffer C, Zeimpekis K, et al. Phantom-based image quality assessment of clinical ^{18}F -FDG protocols in digital PET/CT and comparison to conventional PMT-based PET/CT. *EJNMMI Phys.* 2020;7:1.
9. Alberts I, Prenosil G, Sachpekidis C, et al. Digital versus analogue PET in [^{68}Ga]Ga-PSMA-11 PET/CT for recurrent prostate cancer: a matched-pair comparison. *Eur J Nucl Med Mol Imaging.* 2020;47:614–623.
10. Surti S, Viswanath V, Daube-Witherspoon ME, Conti M, Casey ME, Karp JS. Benefit of improved performance with state-of-the-art digital PET/CT for lesion detection in oncology. *J Nucl Med.* 2020;61:1684–1690.
11. van Sluis J, Boellaard R, Dierckx RAJO, Stormezand GN, Glaudemans AJWM, Noordzij W. Image quality and activity optimization in oncologic ^{18}F -FDG PET using the digital Biograph Vision PET/CT system. *J Nucl Med.* 2020;61:764–771.
12. Zein SA, Karakatsanis N, Issa M, Haj-Ali A, Nehmeh S. Physical performance of a long axial field of view PET scanner prototype with sparser rings configuration: a Monte Carlo simulation study. *Med Phys.* 2020;47:1949–1957.
13. Cherry SR, Jones T, Karp JS, Qi J, Moses WW, Badawi RD. Total-body PET: maximizing sensitivity to create new opportunities for clinical research and patient care. *J Nucl Med.* 2018;59:3–12.
14. Badawi RD, Shi H, Hu P, et al. First human imaging studies with the EXPLORER total-body PET scanner. *J Nucl Med.* 2019;60:299–303.
15. Surti S, Pantel AR, Karp JS. Total body PET: why, how, what for? *IEEE Trans Radiat Plasma Med Sci.* 2020;4:283–292.
16. Zhang J, Maniawski P, Knopp MV. Performance evaluation of the next generation solid-state digital photon counting PET/CT system. *EJNMMI Res.* 2018;8:97.

17. Karp JS, Viswanath V, Geagan MJ, et al. PennPET Explorer: design and preliminary performance of a whole-body imager. *J Nucl Med.* 2020;61:136–143.
18. Conti M, Aykac M, Bal H, et al. Simulation and first measurements on a prototype ultra-long FOV PET/CT scanner. Paper presented at: EANM'20; Virtual Congress; Vienna, Austria; October 23, 2020.
19. Siegel S, Aykac M, Bal H, et al. Preliminary performance of a prototype, one-meter long PET tomograph. Paper presented at: 2020 IEEE Nuclear Science Symposium and Medical Imaging Conference, Virtual; Boston, Massachusetts; November 5, 2020.
20. Reddin JS, Scheuermann JS, Bharkhada D, et al. Performance evaluation of the SiPM-based Siemens Biograph Vision PET/CT system. *2018 IEEE Nucl Sci Symp Med Imaging Conf Rec.* 2018:1–15. doi: 10.1109/NSSMIC.2018.8824710.
21. Zhang Y-Q, Hu P-C, Wu R-Z, et al. The image quality, lesion detectability, and acquisition time of ¹⁸F-FDG total-body PET/CT in oncological patients. *Eur J Nucl Med Mol Imaging.* 2020;47:2507–2515.
22. Spencer BA, Berg E, Schmall JP, et al. Performance evaluation of the uEXPLORER total-body PET/CT scanner based on NEMA NU 2-2018 with additional tests to characterize PET scanners with a long axial field of view. *J Nucl Med.* 2021;62:861–870.
23. *NEMA Standards Publication NU 2-1994: Performance Measurements of Positron Emission Tomographs.* 12th ed. National Electrical Manufacturers Association; 1994.
24. *NEMA Standards Publication NU 2-2018: Performance Measurements of Positron Emission Tomographs (PET).* 18th ed. National Electrical Manufacturers Association; 2018:41.
25. Watson CC, Casey ME, Eriksson L, Mulnix T, Adams D, Bendriem B. NEMA NU 2 performance tests for scanners with intrinsic radioactivity. *J Nucl Med.* 2004; 45:822–826.
26. Bailey DL, Jones T, Spinks TJ. A method for measuring the absolute sensitivity of positron emission tomographic scanners. *Eur J Nucl Med.* 1991;18:374–379.
27. Watson CC. New, faster, image-based scatter correction for 3D PET. *IEEE Trans Nucl Sci.* 2000;47:1587–1594.
28. *IEC Standard 61675-1: Radionuclide Imaging Devices—Characteristics and Test Conditions—Part 1: Positron Emission Tomographs.* International Electrotechnical Commission; 1998:36.
29. Wang G-C, Li X, Niu X, et al. PET timing performance measurement method using NEMA NEC phantom. *IEEE Trans Nucl Sci.* 2016;63:1335–1342.
30. Bharkhada D, Rothfuss H, Conti M. A new method to calculate energy resolution based upon NEC phantom. *2017 IEEE Nucl Sci Symp Med Imaging Conf Rec.* 2017:1–2. doi: 10.1109/NSSMIC.2017.8533007.
31. Alberts I, Hünermund JN, Prenosil G, et al. Clinical performance of long axial field of view PET/CT: a head-to-head intra-individual comparison of the Biograph Vision Quadra with the Biograph Vision PET/CT. *Eur J Nucl Med Mol Imaging.* 2021;48:2395–2404.
32. Conti M. Focus on time-of-flight PET: the benefits of improved time resolution. *Eur J Nucl Med Mol Imaging.* 2011;38:1147–1157.
33. Conti M, Bendriem B. The new opportunities for high time resolution clinical TOF PET. *Clin Transl Imaging.* 2019;7:139–147.
34. Rahmim A, Qi J, Sossi V. Resolution modeling in PET imaging: theory, practice, benefits, and pitfalls. *Med Phys.* 2013;40:064301.